Comparison of Synchronous Reluctance Machines with High-Anisotropy Rotors

Erich Schmidt, *Member*, *IEEE*

Institute of Energy Systems and Electric Drives, Vienna University of Technology, Vienna, Austria

Abstract – **In terms of torque capability, power factor and efficiency, synchronous reluctance machines with high-anisotropy rotors represent an alternative to conventional induction machines. In particular, they have very robust rotors and can therefore operate at constant power in a wider field-weakening range. The paper discusses a comparison of the various machine concepts using an identical machine geometry by using finite element analyses. Experimental results obtained from two machine designs confirm the numerical analyses.**

Index Terms – **Two-axes inductances, Reluctance machine, Permanent magnet machine, Synchronous machine, Finite element analysis**

I. Introduction

In most inverter fed electrical drives, an asynchronous induction machine, a synchronous reluctance machine or a permanent magnet excited synchronous machine is utilized. For an application in a high-performance drive with a wide field-weakening range, both types of synchronous machines are more favourable against induction machines due to their inherent suitability for a position-sensorless control scheme and additionally their more robust rotor [1]–[5].

To achieve a comparable performance, the synchronous reluctance machine should have a high-anisotropy rotor design with internal flux barriers [1], [3], [6], [7]. In comparison to the conventional synchronous reluctance machine, the effective saliency of such rotor designs can be increased by permanent magnets inserted into the flux barriers [7]–[10]. On the other hand, the permanent magnet excited synchronous machine can be realized with such a high-anisotropy rotor design and two possible arrangements of the permanent magnets.

Consequently, there are four different machine concepts which utilize identical stator and rotor geometries. The paper compares these machine designs in terms of the operating behaviour in particular in the field-weakening region. In order to confirm the results from various finite element analyses, measurement data from two rotor designs are presented additionally.

II. Machine Designs

Fig. 1 depicts the various arrangements of high-anisotropy rotors with internal rotor flux barriers concerned:

a. conventional reluctance machine without any permanent magnets, $l_d > l_q$,
b. permanent magnet assisted reluctance machine with $\psi_{Mq} < 0$, $l_d > l_q$,
c. normal-saliency permanent magnet reluctance machine with $\psi_{Md} > 0$, $l_d > l_q$,
d. inverse-saliency permanent magnet reluctance machine with $\psi_{Md} > 0$, $l_d < l_q$.

Fig. 2 depicts stator and high-saliency rotor of the different machine designs concerned. With all four designs, the stator is identical and consists of 24 slots carrying a conventional three-phase full-pitch winding. Slot wedges with a magnetic anisotropy are utilized to minimize the cogging torque of the unskewed machine.

With regard to the circumferential symmetry, only one pole pitch is included in the finite element model. The various angular rotor positions are modelled with a concentric sliding surface inside the air-gap. This facilitates fully independent stator and rotor model parts without any remeshing of the air-gap regions when considering different angular rotor displacements [11]–[13].

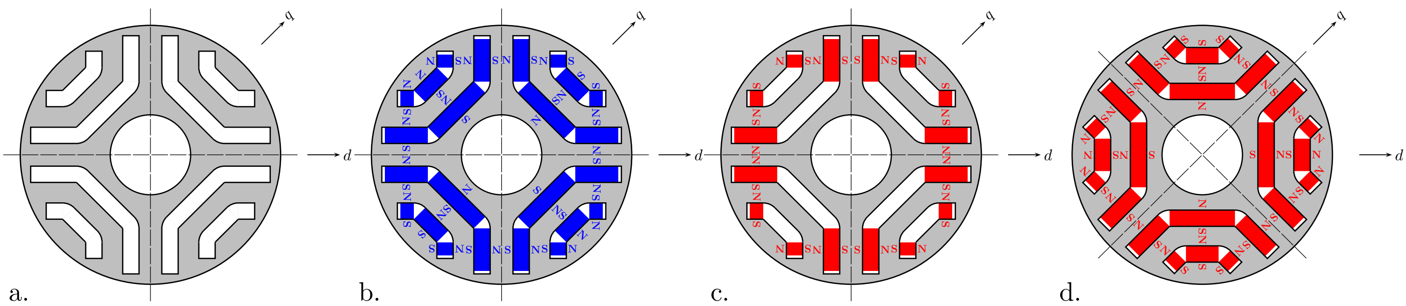

Fig. 1: Comparison of the machine designs: a. conventional reluctance machine,
b. permanent magnet assisted reluctance machine with $\psi_{Mq} < 0$, $l_d > l_q$,
c. normal-saliency permanent magnet reluctance machine with $\psi_{Md} > 0$, $l_d > l_q$,
d. inverse-saliency permanent magnet reluctance machine with $\psi_{Md} > 0$, $l_d < l_q$

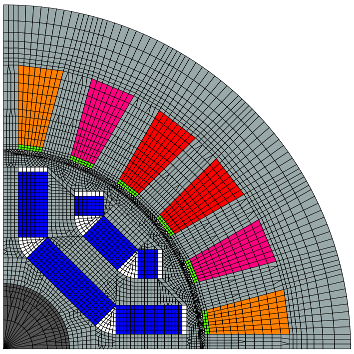

Fig. 2: Finite element model of stator and high-saliency rotor with a sliding surface inside the air-gap

III. Space Vector Calculus

In the dq rotor fixed reference frame, the normalized stator current and stator flux space vectors are given by

$$\underline{i}_{S,dq} = i_S \; e^{\jmath\beta} \; = i_{Sd} + \jmath \, i_{Sq} \;\; , \tag{1}$$

$$\underline{\psi}_{S,dq} = \psi_S \; e^{\jmath\vartheta} = \psi_{Sd} + \jmath \, \psi_{Sq} \;\; , \tag{2}$$

where β,ϑ denote stator current angle and stator flux angle, respectively. By using direct and quadrature axis stator inductances l_d,l_q, the stator linkage flux is defined as

$$\psi_{Sd} = l_d \, i_{Sd} + \psi_{Md} \;\; , \tag{3a}$$

$$\psi_{Sq} = l_q \, i_{Sq} + \psi_{Mq} \;\; . \tag{3b}$$

Consequently, the electromagnetic torque can be written as

$$t_i = -\frac{3}{2} \, \mathrm{Im}\left(\underline{i}^*_{S,dq} \, \underline{\psi}_{S,dq} \right) = \frac{3}{2} \left(\psi_{Sd} \, i_{Sq} - \psi_{Sq} \, i_{Sd} \right) \tag{4}$$
$$= \frac{3}{2} \, i_S^2 \left(\frac{\psi_{Md}}{i_S} \sin\beta - \frac{\psi_{Mq}}{i_S} \cos\beta + \frac{l_d - l_q}{2} \sin 2\beta \right) \;\; .$$

The conventional reluctance machine can be described with a vanishing linkage flux $\psi_M = 0$. With the permanent magnet assisted reluctance machine, $\psi_{Mq} < 0$ represents the permanent magnet linkage flux which counteracts to any quadrature axis stator current $i_{Sq} > 0$. On the other hand, the permanent magnet excited reluctance machine with $\psi_{Md} > 0$ can be designed as either a normal-saliency machine $l_d > l_q$ or an inverse-saliency machine with $l_d < l_q$.

IV. Analysis Results

A. Comparison with Measurements

Fig. 3 and Fig. 4 depict a comparison of measurement data and numerical results from the permanent magnet assisted reluctance machine with $\psi_{Mq} = -0.30$ and the inverse-saliency permanent magnet excited reluctance machine with $\psi_{Md} = 0.66$.

The results discussed further on are evaluated from various finite element analyses. Thereby, the electromagnetic torque is obtained from the Maxwell stresses inside the air-gap. On the other hand, the inductances presented in the following are always apparent inductances obtained by utilizing the frozen permeabilities method.

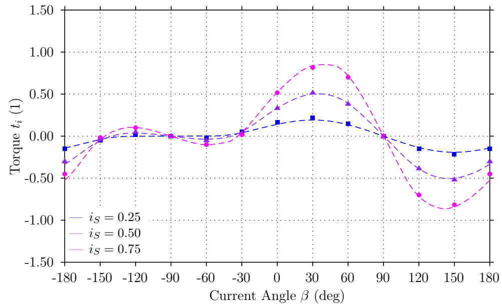

Fig. 3: Torque versus stator current angle β, comparison of numerical results (dashed line) and measurement data (symbols), PM assisted reluctance machine

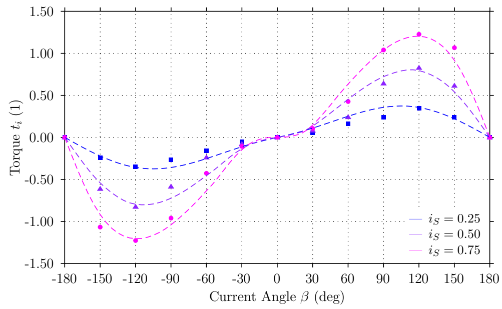

Fig. 4: Torque versus stator current angle β, comparison of numerical results (dashed line) and measurement data (symbols), inverse-saliency PM reluctance machine

B. Reluctance Machines

As from (4), for any given stator current i_S the maximum torque of the conventional reluctance machine is achieved with a current angle of $\cos 2\beta = 0$. On the other hand, for any given stator current i_S the maximum torque of the permanent magnet assisted reluctance machine is achieved with a current angle of

$$\sin\beta = \frac{\psi_{Mq}}{4\,(l_d - l_q)\, i_S} + \sqrt{\left(\frac{\psi_{Mq}}{4\,(l_d - l_q)\, i_S} \right)^2 + \frac{1}{2}} \;\; . \tag{5}$$

Fig. 5 shows the ratio l_d/l_q in dependence on the stator current magnitude i_S with various current angles. Consequently, the permanent magnets with $\psi_{Mq} = -0.30$ significantly increase the saliency-ratio resulting in a wider speed range with constant power. Further, Fig. 6 and Fig. 7 depict the torque t_i with various stator current magnitudes. Finally, Fig. 8 and Fig. 9 show current trajectories result-

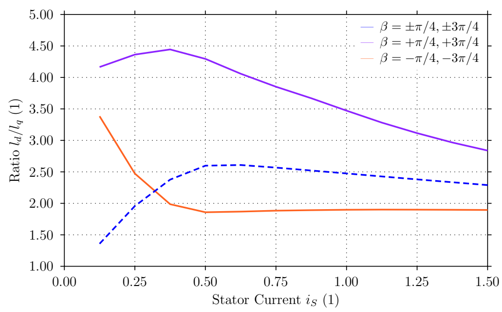

Fig. 5: Ratio l_d/l_q versus stator current magnitude i_S, current angles of $\beta = \pm\pi/4, \pm 3\pi/4$, conventional reluctance machine (dashed line), PM assisted reluctance machine (straight line)

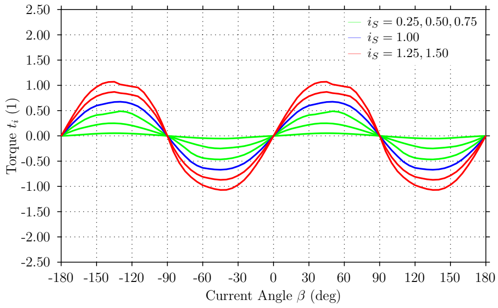

Fig. 6: Torque t_i versus stator current angle β, current magnitudes of $i_S = 0.25 \ldots 1.50$, conventional reluctance machine

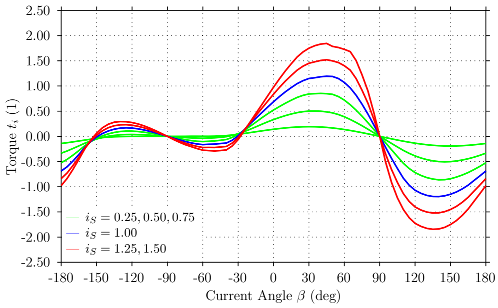

Fig. 7: Torque t_i versus stator current angle β, current magnitudes of $i_S = 0.25 \ldots 1.50$, PM assisted reluctance machine

ing in a contour map of the torque t_i. Obviously, the compensation of the quadrature axis current accomplished by the permanent magnets significantly increases the evolved torque in the range of $0 \leq \beta \leq \pi$.

C. Permanent Magnet Machines

As from (4), for any given stator current i_S in case of the normal-saliency machine the maximum torque of the is achieved with a current angle of

$$\cos\beta = -\frac{\psi_{Md}}{4\,(l_d - l_q)\,i_S} + \sqrt{\left(\frac{\psi_{Md}}{4\,(l_d - l_q)\,i_S}\right)^2 + \frac{1}{2}} \qquad (6)$$

and in case of the inverse-saliency machine

$$\cos\beta = -\frac{\psi_{Md}}{4\,(l_d - l_q)\,i_S} - \sqrt{\left(\frac{\psi_{Md}}{4\,(l_d - l_q)\,i_S}\right)^2 + \frac{1}{2}} \;. \qquad (7)$$

Fig. 10 shows the ratio l_d/l_q of the normal-saliency machine and the ratio l_q/l_d of the inverse-saliency machine with $\psi_{Md} = 0.66$ in dependence on the stator current magnitude i_S with various current angles. Further, Fig. 11 and Fig. 12 depict the torque t_i with various stator current magnitudes. Finally, Fig. 13 and Fig. 14 show current trajectories resulting in a contour map of the torque t_i. Obviously, the inverse-saliency permanent magnet machine yields the highest saliency-ratio resulting in the widest speed range with constant power. On the other hand, the normal-saliency machine acts rather like a reluctance machine because of the high saturation occurring from the flux concentration in the direct axis. Therefore, this arrangement does not present a significant improvement against the arrangement without permanent magnets. Further, the inverse-saliency permanent magnet machine can operate on the

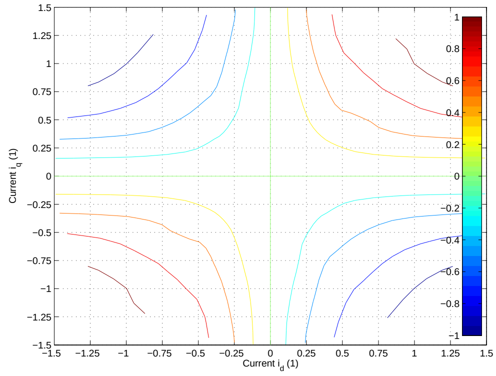

Fig. 8: Contour map of torque t_i versus stator current components i_d,i_q, conventional reluctance machine

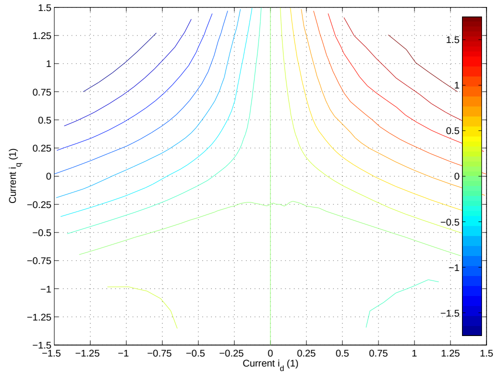

Fig. 9: Contour map of torque t_i versus stator current components i_d,i_q, PM assisted reluctance machine

current limit in a wide speed range. Consequently, it can produce much higher torque values without demagnetizing the permanent magnets in case of an increased current limit of the inverter. Thus, the inverse-saliency machine shows an inherent suitability for electrical drives where short overload operational conditions require high torque values.

V. Conclusion

Synchronous reluctance machines with internal rotor flux barriers are well suited for an application in position-sensorless drives with a wide field-weakening range due to their high effective saliency. By using an identical machine geometry, the conventional reluctance machine and the permanent magnet assisted reluctance machine as well

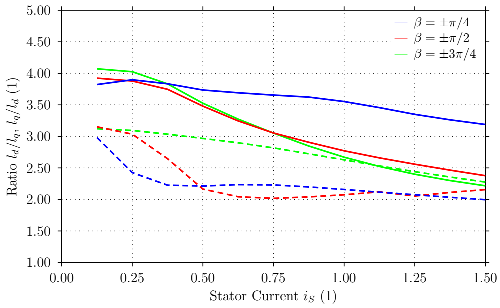

Fig. 10: Ratio l_d/l_q or l_q/l_d versus stator current magnitude i_S, current angles of $\beta = \pm\pi/4, \pm\pi/2, \pm 3\pi/4$, normal-saliency PM reluctance machine (dashed lines), inverse-saliency PM reluctance machine (straight lines)

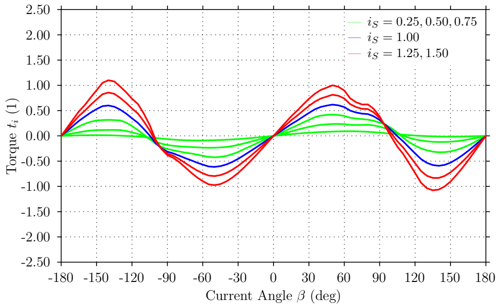

Fig. 11: Torque t_i versus stator current angle β, current magnitudes of $i_S = 0.25 \ldots 1.50$, normal-saliency PM reluctance machine

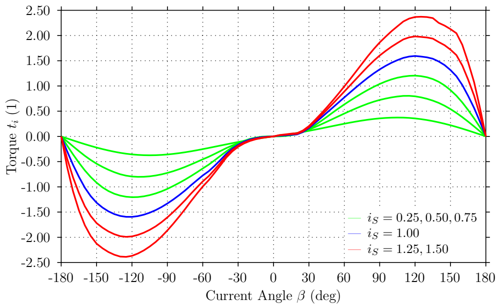

Fig. 12: Torque t_i versus stator current angle β, current magnitudes of $i_S = 0.25 \ldots 1.50$, inverse-saliency PM reluctance machine

as the normal-saliency permanent magnet machine and the inverse-saliency permanent magnet machine are compared against their operational behaviour in particular in the field-weakening range.

The comparison is done in terms of current trajectories with respect to the dq reference frame according to current and voltage limits of the inverter. These diagrams obviously show the advantages of a high saliency ratio l_d/l_q in case of normal-saliency machines or l_q/l_d in case of inverse-saliency machines in particular in the field-weakening region. Thereby, the results from the finite element analyses are successfully compared with measurement data obtained from two machine designs.

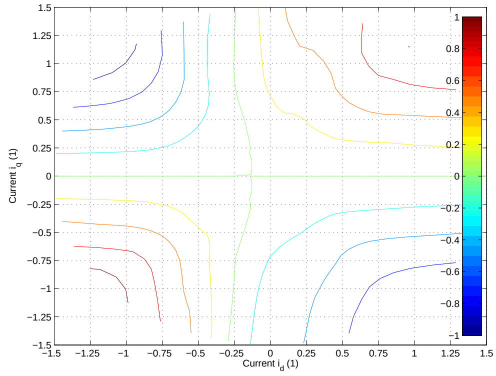

Fig. 13: Contour map of torque t_i versus stator current components i_d,i_q, normal-saliency PM reluctance machine

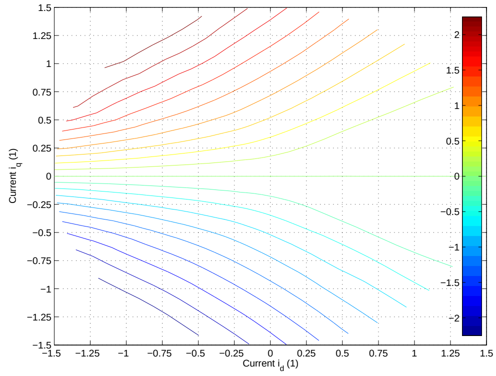

Fig. 14: Contour map of torque t_i versus stator current components i_d,i_q, inverse-saliency PM reluctance machine

References

[1] Vagati A., Fratta A., Franceschini G.: "AC Motors for High-Performance Drives: A Design-Based Comparison". *IEEE Transactions on Industry Applications*, Vol. 32, No. 5, September 1996.

[2] Miller J.M., McClear P.J., Lang J.H.: "Starter-Alternator for Hybrid Electric Vehicle: Comparison of Induction and Variable Reluctance Machines and Drives". *Proceedings of the IEEE Industry Applications Society 33th Annual Meeting*, St.Louis (MO, USA), 1998.

[3] Lovelace E.C., Jahns T.M., Lang J.H.: "Impact of Saturation and Inverter Cost on Interior PM Synchronous Machines Drive Optimization". *IEEE Transactions on Industry Applications*, Vol. 36, No. 3, May 2000.

[4] Haataja J., Pyrhönen J.: "Synchronous Reluctance Motor: An Alternative to Induction Motor". *Proceedings of the 14th International Conference on Electrical Machines, ICEM*, Espoo (Finland), 2000.

[5] De Kock H.W., Kamper M.J., Kennel R.M.: "Anisotropy Comparison of Reluctance and Permanent Magnet Synchronous Machines for Low Speed Position Sensorless Applications". *Proceedings of the 13th Power Electronics and Motion Control Conference, EPE-PEMC*, Poznan (Poland), 2008.

[6] Bianchi N., Bolognani S., Chalmers B.J.: "Comparison of Different Synchronous Motors Drives for Flux-Weakening Applications". *Proceedings of the 13th International Conference on Electric Machines, ICEM*, Instanbul (Turkey), 1998.

[7] Weinmeier P.: *Lagegeberlose hochdynamische Regelung eines Hybrid-Reluktanzmotors im unteren Drehzahlbereich bis zum Stillstand*. Doctoral Thesis (in German), Vienna University of Technology, 1998.

[8] Lee J.H., Kim J.C., Hyun D.S.: "Effect Analysis of Magnet on L_d and L_q Inductance of Permanent Magnet Assisted Synchronous Reluctance Motor using Finite Element Method". *IEEE Transactions on Magnetics*, Vol. 35, No. 3, May 1999.

[9] Schmidt E., Brandl W., Grabner C.: "Design Improvement of Synchronous Reluctance Machines with Internal Rotor Flux Barriers for High-Speed Drives". *Proceedings of the 33rd IEEE Power Electronics Specialists Conference, PESC*, Cairns (QLD, Australia), 2002.

[10] Bianchi N., Bolognani S., Bon D., Dai Pré M.: "Rotor Flux-Barrier Design for Torque Ripple Reduction in Synchronous Reluctance and Permanent Magnet Assisted Synchronous Reluctance Motors". *IEEE Transactions on Industry Applications*, Vol. 45, No. 3, May 2009.

[11] Hameyer K., Belmans R.: *Numerical Modelling and Design of Electrical Machines and Devices*. WIT Press, Southampton (UK), 1999.

[12] De Gersem H., Gyselinck J., Dular P., Hameyer K., Weiland T.: "Comparison of Sliding Surface and Moving Band Techniques in Frequency-Domain Finite Element Models of Rotating Machines". *Proceedings of the 6th International Workshop on Electric and Magnetic Fields (EMF)*, Aachen (Germany), 2003.

[13] De Gersem H., Weiland T.: "Harmonic Weighting Functions at the Sliding Surface Interface of a Finite Element Machine Model Incorporating Angular Displacement". *IEEE Transactions on Magnetics*, Vol. 40, No. 2, March 2004.